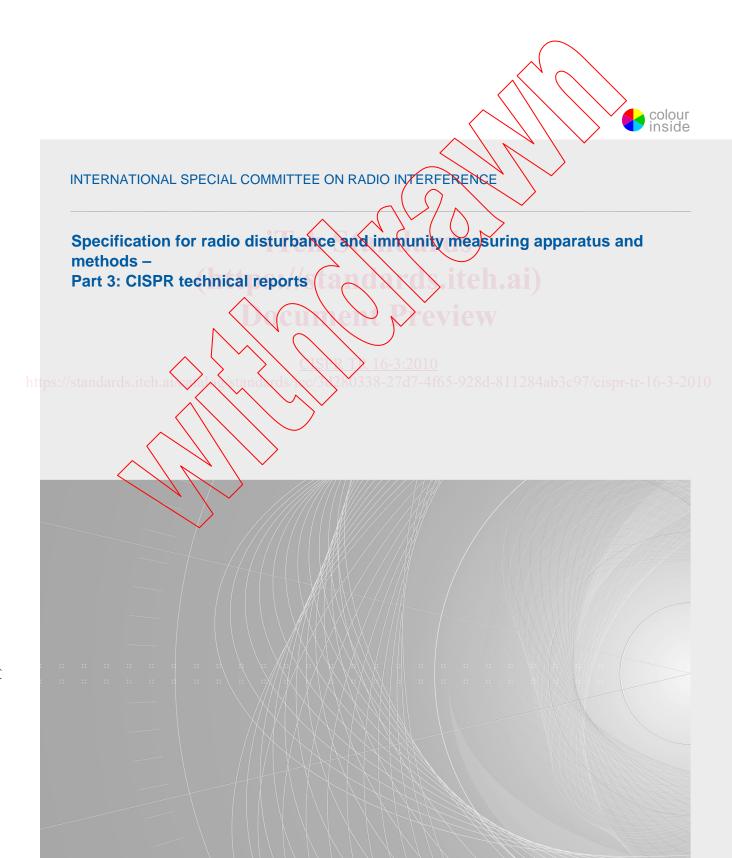




Edition 3.1 2012-07

TECHNICAL REPORT





THIS PUBLICATION IS COPYRIGHT PROTECTED Copyright © 2012 IEC, Geneva, Switzerland

All rights reserved. Unless otherwise specified, no part of this publication may be reproduced or utilized in any form or by any means, electronic or mechanical, including photocopying and microfilm, without permission in writing from either IEC or IEC's member National Committee in the country of the requester.

If you have any questions about IEC copyright or have an enquiry about obtaining additional rights to this publication, please contact the address below or your local IEC member National Committee for further information.

IEC Central Office Tel.: +41 22 919 02 11 3, rue de Varembé Fax: +41 22 919 03 00

CH-1211 Geneva 20 info@iec.ch Switzerland www.iec.ch

About the IEC

The International Electrotechnical Commission (IEC) is the leading global organization that prepares and publishes International Standards for all electrical, electronic and related technologies.

About IEC publications

The technical content of IEC publications is kept under constant review by the IEC. Please make sure that you have the latest edition, a corrigenda or an amendment might have been published.

Useful links:

IEC publications search - www.iec.ch/searchpub

The advanced search enables you to find IEC publications by a variety of criteria (reference number, text, technical committee,...).

It also gives information on projects, replaced and withdrawn publications.

IEC Just Published - webstore.iec.ch/justpublished

Stay up to date on all new IEC publications. Just Published details all new publications released Available on-line and also once a month by email.

Electropedia www.electropedia.org

The world's leading online dictionary of electronic and electrical terms containing more than 30 000 terms and definitions in English and French, with equivalent terms in additional languages. Also known as the International Electrotechnical Vocabulary (IEV) on-line.

Customer Service Centre - webstore.iec.ch/csc

If you wish to give us your feedback on this publication need further assistance, please contact the Customer Service Centre: csc@iec.ch.

X 16-3:2010

https://standards.iteh.ai



CISPR/TR 16-3

Edition 3.1 2012-07

TECHNICAL REPORT



INTERNATIONAL ELECTROTECHNICAL COMMISSION

ICS 33.100.10, 33.100.20 ISBN 978-2-8322-0282-1

Warning! Make sure that you obtained this publication from an authorized distributor.

CONTENTS

FOF	DREWORD1			14
1	Scop	e		16
2	Norm	ative re	eferences	16
3	Term	s. defin	itions and abbreviations	17
	3.1	•	and definitions	
	3.2		/iations	
4	_		ports	
	4.1	Correlation between measurements made with apparatus having characteristics differing from CISPR characteristics and measurements made with CISPR apparatus		20
		4.1.1	General	
		4.1.2	Critical interference-measuring instrument parameters	
		4.1.3	Impulse interference – correlation factors	23
		4.1.4	Random noise	25
		4.1.5	The root mean square (rms) detector	25
		4.1.6	Discussion Application to typical noise sources Conclusions	25
		4.1.7	Application to typical noise sources	25
	4.0	4.1.8	Conclusionsrence simulators	26
	4.2		Constal	27
		4.2.1 4.2.2	General Types of interference signals	27
		4.2.2	Circuits for simulating broadband interference	
	4.3	_	onship between limits for open-area test site and the reverberation	20
	4.3	chamb		32
		4.3.1	General	
		4.3.2	Correlation between measurement results of the reverberation chamber and OATS	
		4.3.3	Limits for use with the reverberation chamber method	33
		4.3.4	Rrocedure for the determination of the reverberation chamber limit	33
	4.4 <	induce	cterization and classification of the asymmetrical disturbance source of in telephone subscriber lines by AM broadcasting transmitters in the W and SW bands	24
		4.4.1	General	
		4.4.2	Experimental characterization	
		4.4.3	Prediction models and classification	
		4.4.4	Characterization of the immunity-test disturbance source	
	4.5		tability of radiation in vertical directions at frequencies above 30 MHz	
		4.5.1	Summary	
		4.5.2	Range of application	
		4.5.3	General	
		4.5.4	Method used to calculate field patterns in the vertical plane	
		4.5.5	Limitations of predictability of radiation at elevated angles	
		4.5.6	Differences between the fields over a real ground and the fields over a perfect conductor	
		4.5.7	Uncertainty ranges	
		4.5.8	Conclusions	

5 Bac	ground and history of CISPR		231
5.1	The history of CISPR		231
	5.1.1 The early years: 1934-	1984	231
	• •	984 to 1998	
	' '		233
5.2	power produced by electrical h	ethod of measurement of the interference ousehold and similar appliances in the VHF	234
	5.2.1 Historical detail		234
	5.2.2 Development of the me	thod	235
		ormula	237
Annex B	(informative) The field-strength	distribution	241
Annex C	(informative) The induced asyn	nmetrical open-circuit voltage distribution	245
Annex D	(informative) The outlet-voltage	e distribution	248
Annex E	(informative) Some mathematic	al relations	250
	(informative) Harmonic fields rant over real ground	idiated at elevated angles from 27 MHz ISM	252
Bibliogra	phy		258
Figure 1	 Relative response of various 	letectors to impulse interference	22
Figure 2	– Pulse rectificati <mark>øn coefficie</mark> nt	P(a)	23
Figure 3	- Pulse repetition frequency	(e) / eview	24
Figure 4	 Block diagram and waveforms 	of a simulator generating noise bursts	30
	- Block diagram of a simulator	penerating noise bursts according to the pulse	31
Figure 6	- Details of a typical output stag	/ Je	32
Figure 7 versus t	 Scatter plot of the measured of e calculated outdoor magnetic f 	outdoor magnetic field strength $H_{ m O}$ (dB μ A/m) ield strength $H_{ m C}$ dB(μ A/m)	36
Figure 8	Measured outdoor magnetic v	ersus distance, and probability of the building-	37
		ouilding-effect parameter A _b dB	
		ntenna factor G_{O} dB(Ω m) versus the indoor	39
Figure 1	- Normal probability plots of th	e antenna factors	40
Figure 1	2 – Normal probability plot of the	equivalent asymmetrical resistance R_a dB(Ω)	43
Figure 1	B – Examples of the frequency d	ependence of some parameters	44
Figure 1	I – Example of the frequency his	stogram $\Delta N(E_{\mathbf{O}}, \Delta E_{\mathbf{O}})$	49
Figure 1 maximu	$S-E$ Example of $n_{\mathbf{m}}(E_{0})$, i.e. the on field strength E_{0} resulting from	listribution of the outlets experiencing a a given number of transmitters in (or near)	
Figure 1	6 – Example of the number of ou	tlets with an induced asymmetrical open- ee Table 10)	
Figure 1	' - Examples of number (left-ha	nd scale) and relative number (right-hand	

Figure 18 – Vertical polar patterns of horizontally polarized E_{χ} field strengths emitted around small vertical loop (horizontal magnetic dipole) over three different types of real ground61	
Figure 19 – Height scan patterns of vertically oriented E_z field strengths emitted from small vertical loop (horizontal magnetic dipole) over three different types of real ground61	
Figure 20 – Vertical polar patterns of horizontally polarized E_{χ} field strengths emitted around small vertical loop (horizontal magnetic dipole), over three different types of real ground	;
Figure 21 – Vertical polar patterns of vertically oriented E_Z field strengths emitted around small vertical loop (horizontal magnetic dipole) over three different types of real ground63	;
Figure 22 – Height scan patterns of vertically oriented E_z field strengths emitted at 1 000 MHz from the small vertical loop (horizontal magnetic dipole), at horizontal distance of 10 m, 30 m and 300 m in the Z-X plane over three different types of real ground	ļ
Figure 23 – Vertical polar patterns of horizontally polarized E_χ and vertically oriented E_Z field strengths emitted around small horizontal electric dipole, in Y-Z and Z-X planes respectively	j
Figure 24 – Height scan patterns of horizontally polarized E _x field strengths emitted from small horizontal electric dipole	j
Figure 25 – Vertical polar patterns of horizontally polarized E_{χ} and vertically oriented E_{Z} field strengths emitted around small horizontal electric dipole in χ -Z and Z-X planes respectively)
Figure 26 – Height scan patterns of horizontally polarized E_{χ} field strengths emitted small horizontal electric dipole)
Figure 27 – Vertical polar patterns of horizontally polarized E_x and vertically oriented E_z field strengths emitted around small vertical loop (prorizontal magnetic dipole) in Y-Z and Z-X planes respectively)
Figure 28 – Height scan patterns of vertically oriented E_z and horizontally oriented E_x field strengths emitted from small vertical loop (horizontal magnetic dipole)70)
Figure 29 – Vertical polar patterns of vertically oriented E_z and horizontally oriented E_x field strengths emitted around small vertical electric dipole73	5-
Figure 30 – Height scan patterns of vertically oriented E_z and horizontally oriented E_x field strengths emitted from small vertical electric dipole73	;
Figure 31 Vertical polar patterns of horizontally polarized E_X and vertically oriented E_Z field strengths emitted around small vertical loop (horizontal magnetic dipole) in Y-Z and Z-X planes respectively74	ļ
Figure 32 – Height scan patterns of vertically oriented E_z and horizontally oriented E_x field strengths emitted from small vertical loop (horizontal magnetic dipole)74	Ļ
Figure 33 – Vertical polar patterns of horizontally polarized <i>E</i> -field strength emitted around small horizontal loop (vertical magnetic dipole)75	;
Figure 34 – Height scan patterns of horizontally polarized <i>E</i> -field strength emitted from small horizontal loop (vertical magnetic dipole)	;
Figure 35 – Vertical polar patterns of vertically oriented $E_{\mathcal{Z}}$ and horizontally oriented $E_{\mathcal{X}}$ field strengths emitted around small vertical electric dipole78	;
Figure 36 – Height scan patterns of vertically oriented $E_{\mathcal{Z}}$ and horizontally oriented $E_{\mathcal{X}}$ field strengths emitted from the small vertical electric dipole78	;
Figure 37 – Vertical polar patterns of horizontally polarized E_χ and vertically oriented E_Z field strengths emitted around small vertical loop (horizontal magnetic dipole) in Y-Z and Z-X planes respectively79)
Figure 38 – Height scan patterns of vertically oriented E_z and horizontally oriented E_x field strengths emitted from small vertical loop (horizontal magnetic dipole)79)

Figure 39 – Vertical polar patterns of horizontally polarized <i>E</i> -field strength emitted around small horizontal loop (vertical magnetic dipole)	.80
Figure 40 – Height scan patterns of horizontally polarized <i>E</i> -field strength emitted from small horizontal loop (vertical magnetic dipole)	.80
Figure 41 – Vertical polar patterns of horizontally polarized <i>E</i> -field strength emitted around the small horizontal loop (vertical magnetic dipole)	.83
Figure 42 – Height scan patterns of horizontally polarized <i>E</i> -field strength emitted from small horizontal loop (vertical magnetic dipole)	.83
Figure 43 – Height scan patterns of horizontally polarized <i>E</i> -field strength emitted from small horizontal loop (vertical magnetic dipole)	.87
Figure 44 – Height scan patterns of the vertical component of the <i>E</i> -fields emitted from a small vertical electric dipole	.90
Figure 45 – Height scan patterns of the vertical component of the E-fields enlitted from a small vertical electric dipole	.90
Figure 46 – Height scan patterns of the horizontally polarized Effets emitted in the vertical plane normal to the axis of a small horizontal electric dipole	.92
Figure 47 – Height scan patterns of the horizontally polarized E-fields emitted in the vertical plane normal to the axis of a small horizontal electric dipole	.92
Figure 48 – Ranges of uncertainties in the predictability of radiation in vertical directions from electrically small sources located at a height of 1 m or 2 m above ground	.94
Figure 49 – Ranges of uncertainties in the predictability of radiation in vertical directions from electrically small sources located at a height of 1 m or 2 m above ground	.95
Figure 50 – Ranges of uncertainties in the predictability of radiation in vertical directions from electrically small sources located at a height of 1 m or 2 m above ground	.96
Figure 51 – Geometry of the small vertical electric dipole model	
Figure 52 – Geometry of the small horizontal electrical dipole model	100
Figure 53 – Geometry of the small horizontal magnetic dipole model (small vertical loop)	100
Figure 54 – Geometry of the small vertical magnetic dipole model (small horizontal loop)	100
Figure 55 – Ranges of errors in the predictability of radiation in vertical directions from electrically small sources located close to the ground, based on measurements of the horizontally oriented X-field near ground at a distance of 30 m from the sources	108
Figure 56 – Ranges of errors in the predictability of radiation in vertical directions from electrically small sources located close to the ground, based on measurements of the horizontally oriented H -field at the ground supplemented with measurements of the vertically oriented H -field in a height scan up to 6 m at a distance of 30 m from the sources.	109
Figure 57 – Vertical radiation patterns of horizontally oriented <i>H</i> -fields emitted by a small vertical electric dipole located close to the ground	111
Figure 58 – Vertical radiation patterns of horizontally oriented <i>H</i> -fields emitted by a small vertical electric dipole located close to the ground	111
Figure 59 – Vertical radiation patterns of <i>E</i> -fields emitted by a small vertical electric dipole located close to the ground	112
Figure 60 – Vertical radiation patterns of the <i>E</i> -fields emitted by a small vertical electric dipole located close to the ground	112
Figure 61 – Vertical radiation patterns of the <i>H</i> -fields emitted by a small horizontal electric dipole located close to the ground	113

Figure 62 – Influence of a wide range of values of the electrical constants of the ground on the vertical radiation patterns of the horizontally oriented <i>H</i> -fields emitted by a small horizontal electric dipole located close to the ground
Figure 63 – Vertical radiation patterns of the horizontally oriented <i>H</i> -fields emitted by a small horizontal electric dipole located close to the ground
Figure 64 – Vertical radiation patterns of the <i>E</i> -fields emitted by a small horizontal electric dipole located close to the ground
Figure 65 – Vertical radiation patterns of the <i>E</i> -fields emitted by a small horizontal electric dipole located close to the ground
Figure 66 – Vertical radiation patterns of <i>H</i> -fields emitted by small horizontal magnetic dipole (vertical loop) located close to ground
Figure 67 – Vertical radiation patterns of the horizontally oriented <i>H</i> -fields emitted by a small horizontal magnetic dipole (vertical loop) located close to the ground116
Figure 68 – Vertical radiation patterns of the horizontally oriented H fields emitted by a small horizontal magnetic dipole (vertical loop) located close to the ground116
Figure 69 – Vertical radiation patterns of the <i>E</i> -fields emitted by a small horizontal magnetic dipole (vertical loop) located close to the ground
Figure 70 – Vertical radiation patterns of the <i>E</i> -fields emitted by a small horizontal magnetic dipole (vertical loop) located close to the ground
Figure 71 – Vertical radiation patterns of the <i>H</i> -fields emitted by a small vertical magnetic dipole (horizontal loop) located close to the ground
Figure 72 – Vertical radiation patterns of the H-fields emitted by a small vertical magnetic dipole (horizontal loop) located close to the ground
Figure 73 – Vertical radiation patterns of the <i>H</i> -fields emitted by a small vertical magnetic dipole (horizontal loop) located close to the ground
Figure 74 – Vertical radiation patterns of the H-fields emitted by a small vertical magnetic dipole (horizontal loop) located close to the ground
Figure 75 – Vertical radiation pattern of the E-field emitted by a small vertical magnetic dipole (horizontal loop) located close to the ground
Figure 76 – Vertical radiation patterns of the <i>E</i> -fields emitted by a small vertical magnetic dipole (horizontal loop) located close to the ground
Figure 77 – Vertical radiation patterns of the horizontally oriented <i>H</i> -fields emitted by a small vertical electric dipole located close to the ground
Figure 78 – Vertical radiation patterns of the <i>E</i> -fields emitted by a small vertical electric dipole located close to the ground
Figure 79 – Vertical radiation patterns of the <i>E</i> -fields emitted by a small vertical electric dipole located close to the ground122
Figure 80 – Vertical radiation patterns of the <i>H</i> -fields emitted by a small horizontal electric dipole located close to the ground122
Figure 81 – Vertical radiation patterns of the horizontally oriented <i>H</i> -fields emitted by a small horizontal electric dipole located close to the ground
Figure 82 – Vertical radiation patterns of the <i>E</i> -fields emitted by a small horizontal electric dipole located close to the ground123
Figure 83 – Vertical radiation patterns of the <i>E</i> -fields emitted by a small horizontal electric dipole located close to the ground
Figure 84 – Vertical radiation patterns of the <i>H</i> -fields emitted by a small horizontal magnetic dipole (vertical loop) located close to the ground
Figure 85 – Vertical radiation patterns of the horizontally oriented <i>H</i> -fields emitted by a small horizontal magnetic dipole (vertical loop) located close to the ground
Figure 86 – Vertical radiation patterns of the horizontally oriented <i>H</i> -fields emitted by a small horizontal magnetic dipole (vertical loop) located close to the ground

Figure 87 – Vertical radiation patterns of the <i>E</i> -fields emitted by a small horizontal magnetic dipole (vertical loop) located close to the ground
Figure 88 – Vertical radiation patterns of the <i>E</i> -fields emitted by a small horizontal magnetic dipole (vertical loop) located close to the ground
Figure 89 – Vertical radiation patterns of the <i>H</i> -fields emitted by a small vertical magnetic dipole (horizontal loop) located close to the ground127
Figure 90 – Vertical radiation patterns of the <i>H</i> -fields emitted by a small vertical magnetic dipole (horizontal loop) located close to the ground127
Figure 91 – Vertical radiation patterns of the <i>H</i> -fields emitted by a small vertical magnetic dipole (horizontal loop) located close to the ground128
Figure 92 – Vertical radiation patterns of the <i>E</i> -fields emitted by a small vertical magnetic dipole (horizontal loop) located close to the ground128
Figure 93 – Vertical radiation patterns of the horizontally oriented <i>H</i> -fields emitted by a small vertical electric dipole located close to the ground
Figure 94 – Vertical radiation patterns of the <i>E</i> -fields emitted by a small vertical electric dipole located close to the ground
Figure 95 – Vertical radiation patterns of the <i>E</i> -fields emitted by a small vertical electric dipole located close to the ground
Figure 96 – Vertical radiation patterns of the <i>H</i> -fields emitted by a small horizontal electric dipole located close to the ground
Figure 97 – Vertical radiation patterns of the E-fields emitted by a small horizontal electric dipole located close to the ground
Figure 98 – Vertical radiation patterns of the <i>E</i> -fields emitted by a small horizontal electric dipole located close to the ground
Figure 99 – Vertical radiation patterns of the <i>H</i> -field emitted by a small horizontal magnetic dipole (vertical loop) located close to the ground
Figure 100 – Vertical radiation patterns of the vertically polarized <i>E</i> -fields emitted by a small horizontal magnetic dipole (vertical loop) located close to the ground
Figure 101 – Vertical radiation patterns of the <i>H</i> -field emitted by a small vertical 7/cispr-tr-16-3-20 magnetic dipole (horizontal loop) located close to the ground
Figure 102 – Vertical radiation patterns of the <i>E</i> -fields emitted by a small vertical magnetic dipole (horizontal loop) located close to the ground
Figure 103 – Vertical radiation patterns of the horizontally oriented <i>H</i> -fields emitted by a small vertical electric dipole located close to the ground
Figure 104 - Vertical radiation patterns of the vertically polarized <i>E</i> -fields emitted by a small vertical electric dipole located close to the ground
Figure 105 – Vertical radiation patterns of the <i>H</i> -fields emitted by a small horizontal electric dipole located close to the ground135
Figure 106 – Vertical radiation patterns of the horizontally oriented <i>H</i> -fields emitted by a small horizontal electric dipole located close to the ground
Figure 107 – Influence of a wide range of values of the electrical constants of the ground on the vertical radiation patterns of the horizontally oriented <i>H</i> -fields emitted by a small horizontal electric dipole located close to the ground
Figure 108 – Vertical radiation patterns of the vertically polarized <i>E</i> -fields emitted by a small horizontal electric dipole located close to the ground
Figure 109 – Vertical radiation patterns of the <i>H</i> -fields emitted by a small horizontal magnetic dipole (vertical loop) located close to the ground
Figure 110 – Vertical radiation patterns of the vertically polarized <i>E</i> -fields emitted by a small horizontal magnetic dipole (vertical loop) located close to the ground137
Figure 111 – Vertical radiation patterns of the <i>H</i> -fields emitted by a small vertical magnetic dipole (horizontal loop) located close to the ground

	Vertical radiation patterns of the <i>E</i> -fields emitted by a small vertical ole (horizontal loop) located close to the ground	138
	Set-up for measuring communication quality degradation of a wireless	139
	APD characteristics of disturbance	
Figure 115 –	Wireless LAN throughput influenced by noise	142
Figure 116 –	Set-up for measuring the communication quality degradation of Bluetooth	143
Figure 117 –	APD of disturbance of actual MWO (2 441MHz)	143
Figure 118 –	APD characteristics of disturbance (2 460 MHz)	144
	Throughput of Bluetooth influenced by noise	
Figure 120 –	Set-up for measuring the BER of W-CDMA	147
	APD characteristics of disturbance	148
Figure 122 –	BER of W-CDMA caused by radiation noise	149
Figure 123 –	Set-up for measuring the PHS throughput	150
Figure 124 –	Set-up for measuring the BER of PHS	150
	APD characteristics of disturbance	
Figure 126 –	PHS throughput caused by radiation	152
Figure 127 –	BER of PHS caused by radiation noise	153
-	Correlation of the disturbance voltages with the system performance	154
Figure 129 –	Correlation of the disturbance voltages with the system performance	155
Figure 130 –	Correlation of the disturbance voltages with the system performance	155
Figure 131 – (<i>C/N</i> ₀)	Correlation of the disturbance voltages with the system performance	156
Figure 132 – (<i>C/N</i> ₀)	Correlation of the disturbance voltages with the system performance	156
Figure 133 – a PHS or W-	Experimental set-up for measuring communication quality degradation of CDMA	157
	Simulation set-up for estimating communication quality degradation of a MA	157
-	APD of pulse disturbance	158
Figure 136 - (Carrier pow	BER degradation of PHS and W-CDMA caused by repetition pulse er, 35 dBm)	158
Figure 137 –	Evaluation method of the correlation between BER and APD	159
Figure 138 –	Correlation between measured Δ $L_{\sf BER}$ and Δ $L_{\sf APD}$	159
Figure 139 –	Correlation between measured page and papp	160
	Weighting curves of quasi-peak measuring receivers for the different nges as defined in CISPR 16-1-1	161
	Weighting curves for peak, quasi-peak, rms and linear average detectors ands C and D	162
	Test setup for the measurement of the pulse weighting characteristics of ocommunication system	163
	Example of an interference spectrum: pulse modulated carrier with a on of 0,2 μs and a PRF < 10 kHz	164
	The rms and peak levels for constant BEP for three $K=3$, convolutional erent rate	166

Figure 145 – The rms and peak levels for constant BEP for two rate ½, convolutional code	57
Figure 146 – Test setup for the measurement of weighting curves for Digital Radio Mondiale (DRM)	9
Figure 147 – Weighting characteristics for DRM signals for various pulse widths of the pulse-modulated carrier	0
Figure 148 – Weighting characteristics for DRM protection level 0: average of results for two receivers	'1
Figure 149 – Weighting characteristics for DRM protection level 1: average of results for two receivers	'1
Figure 150 – Weighting characteristics for DVB-T with 64 QAM 2k, CR 3/4 (as used in France and UK)	'3
Figure 151 – Weighting characteristics for DVB-T with 64 QAM 8k, CR 3/4 (as used in Spain)	' 4
Figure 152 – Weighting characteristics for DVB-T with 16 QAM 8k, CR 2/3 (as used in Germany)	'4
Figure 153 – Average weighting characteristics of 6 receiver types for DVB-T with 16QAM	'5
Figure 154 – Average weighting characteristics of 6 receiver types for DVB-T with 64QAM	6
Figure 155 – Weighting characteristics for DAB (signal level -71 dBm) with a flat response down to approximately 1 kHz	
Figure 156 – Weighting characteristics for DAB: average of two different commercial receiver types	7
Figure 157 – Weighting characteristics for TETRA (signal level – 80 dBm) for a code rate of 1	'8
Figure 158 – Weighting characteristics for RBER 1b of GSM (signal level –90 dBm)17	'9
Figure 159 – Weighting characteristics for RBER 2 of GSM	
computed for GSM using COSSAP	0
Figure 161 – Rms and quasi-peak values of pulse level for constant effect on FM radio reception	0
Figure 162 - Weighting characteristics for RBER 1b of GSM (signal level -90 dBm)18	
Figure 163 - Weighting characteristics for DECT (signal level -83 dBm)18	2
Figure 164 – Weighting characteristics for IS-95 (signal level -97 dBm) with comparatively high immunity to interference	3
Figure 165 – Weighting characteristics for J-STD 008 (signal level –97 dBm)18	
Figure 166 – Weighting characteristics for the Frame Error Ratio (FER) of CDMA2000 (measured at a receive signal level of –112 dBm) for a low data rate of 9,6 kb/s	4
Figure 167 – Weighting characteristics for the Frame Error Ratio (FER) of CDMA2000 (measured at a receive signal level of –106 dBm) for two different data rates (9,6 kb/s and 76,8 kb/s)	55
Figure 168 – The proposed rms-average detector for CISPR Bands C and D with a corner frequency of 100 Hz18	
Figure 169 – Rms-average detector function by using an rms detector followed by a linear average detector and peak reading	
Figure 170 – Rms-average weighting functions for CISPR Bands A, B, C/D and E for	
the shortest pulse widths allowed by the measurement bandwidths18	9

Figure 180 – Position of the reference planes for the measurement with SQLT calibration and ABCD transformation to Z _{ref} level	19 19 19 19 20
Figure 174 – Conformal mapping between z-plane and f-plane	19 19 19 20
device-under-test. Figure 176 – Basic model for the TRL calibration. Figure 177 – The four calibration configurations necessary for the TRL calibration. Figure 178 – Measurement of CMAD characteristics. Figure 179 – Preliminary measurements of the test set-up. Figure 180 – Position of the reference planes for the measurement with SQLT calibration and ABCD transformation to Z _{ref} level. Figure 181 – Superheterodyne EMI receiver Figure 182 – An example spectrogram Z[m,k]. Figure 183 – Sidelobe effect due to the finite length of window. Figure 184 – Measurement error for a single pulse. Figure 185 – IF signal for different overlapping factors for the same sequence of pulses. Figure 186 – FFT-based baseband system. Figure 187 – Real-time FFT-based measuring instrument. Figure 189 – Short time fast Fourier transform – An example of implementation. Figure 190 – Floating point analogue to digital conversion. Figure 191 – Example of a 120 kHz Gaussian filter. Figure 192 – Essential parts of an FF N-based heterodyne receiver. Figure 193 – Dynamic range for broadband emission as measured with the peak detector. Figure 194 – Set-up of FFT-based system type 2. Figure 195 – FFT Software ("FFTemi") screen shot. Figure 196 – Example of pulse generator measurement with antenna. Figure 197 – Radiated emission measurement of a motor – peak detector. Figure 198 – Angular characterization of a PC. Figure 199 – Example FFT IF analysis display.	19 20 20
Figure 177 – The four calibration configurations necessary for the TRL calibration Figure 178 – Measurement of CMAD characteristics Figure 179 – Preliminary measurements of the test set-up Figure 180 – Position of the reference planes for the measurement with SQLT calibration and ABCD transformation to Z _{Tef} level Figure 181 – Superheterodyne EMI receiver Figure 182 – An example spectrogram Z[m,k]. Figure 183 – Sidelobe effect due to the finite length of window. Figure 184 – Measurement error for a single pulse Figure 185 – IF signal for different overlapping factors for the same sequence of pulses Figure 187 – Real-time FFT-based measuring instrument Figure 189 – Short time fast Fourier transform – An example of implementation Figure 190 – Floating-point analogue to digital conversion Figure 191 – Example of a 120 kHz Gaussian filter Figure 193 – Dynamic range for broadband emission as measured with the peak detector Figure 194 – Set-up of FFT-based system type 2 Figure 195 – FRT Software ("FFTemi") screen shot Figure 197 – Radiated emission measurement with antenna Figure 198 – Angular characterization of a PC Figure 199 – Example of pulse generator measurement with antenna Figure 199 – Example of pulse generator measurement with antenna Figure 199 – Example of pulse generator measurement with antenna Figure 199 – Example of pulse generator measurement with antenna Figure 199 – Example of pulse generator measurement with antenna Figure 199 – Example FFT IF analysis display	20 20
Figure 178 – Measurement of CMAD characteristics Figure 179 – Preliminary measurements of the test set-up. Figure 180 – Position of the reference planes for the measurement with SQLT calibration and ABCD transformation to Zref level. Figure 181 – Superheterodyne EMI receiver. Figure 182 – An example spectrogram Z[m,k]. Figure 183 – Sidelobe effect due to the finite length of window. Figure 184 – Measurement error for a single pulse. Figure 185 – IF signal for different overlapping factors for the same sequence of pulses. Figure 186 – FFT-based baseband system. Figure 187 – Real-time FFT-based measuring instrument. Figure 189 – Short time fast Fourier transform – An example of implementation. Figure 190 – Floating-point analogue to digital conversion. Figure 191 – Example of a 120 kHz Gausstan filter. Figure 192 – Essential parts of an FFT-based heterodyne receiver. Figure 193 – Dynamic range for broadband emission as measured with the peak detector. Figure 194 – Set-up of FFT-based system type 2. Figure 195 – FFT Software ("FFTemi") screen shot. Figure 196 – Example of pulse generator measurement with antenna. Figure 197 – Radiated emission measurement of a motor – peak detector. Figure 198 – Angular characterization of a PC. Figure 199 – Example FFT IF analysis display.	20
Figure 179 – Preliminary measurements of the test set-up Figure 180 – Position of the reference planes for the measurement with SQLT calibration and ABCD transformation to Z _{ref} level Figure 181 – Superheterodyne EMI receiver Figure 182 – An example spectrogram Z[m,k] Figure 183 – Sidelobe effect due to the finite length of window Figure 185 – IF signal for different overlapping factors for the same sequence of pulses Figure 186 – FFT-based baseband system Figure 187 – Real-time FFT-based measuring instrument Figure 189 – Short time fast Fourier transform – An example of implementation Figure 190 – Floating-point analogue-to digital conversion Figure 191 – Example of a 120 kHz Gaussian filter Figure 192 – Essential parts of an FFT-based heterodyne receiver Figure 194 – Set-up of FFT-based system type 2 Figure 195 – FFT Software ("FFTemi") screen shot Figure 196 – Example of pulse generator measurement with antenna Figure 197 – Radiated emission measurement of a motor – peak detector Figure 198 – Angular characterization of a PC Figure 199 – Example FFT IF analysis display	
Figure 180 – Position of the reference planes for the measurement with SQLT calibration and ABCD transformation to Z _{ref} level	
calibration and ABCD transformation to Z _{ref} level	20
Figure 182 – An example spectrogram Z[m,k]	20
Figure 183 – Sidelobe effect due to the finite length of window	20
Figure 184 – Measurement error for a single pulse	21
Figure 185 – IF signal for different overlapping factors for the same sequence of pulses. Figure 186 – FFT-based baseband system. Figure 187 – Real-time FFT-based measuring instrument. Figure 188 – Digital down converter. Figure 189 – Short time fast Fourier transform – An example of implementation. Figure 190 – Floating-point analogue-to digital conversion. Figure 191 – Example of a 120 kHz Gaussian filter. Figure 192 – Essential parts of an FFT-based heterodyne receiver. Figure 193 – Dynamic range for broadband emission as measured with the peak detector. Figure 194 – Set-up of FFT-based system type 2. Figure 195 – FFT Software ("FFTemi") screen shot. Figure 196 – Example of pulse generator measurement with antenna. Figure 197 – Radiated emission measurement of a motor – peak detector. Figure 198 – Angular characterization of a PC. Figure 199 – Example FFT IF analysis display.	21
Figure 186 – FFT-based baseband system Figure 187 – Real-time FFT-based measuring instrument Figure 188 – Digital down converter Figure 189 – Short time fast Fourier transform – An example of implementation Figure 190 – Floating-point analogue to digital conversion Figure 191 – Example of a 120 kHz Gaussian filter Figure 192 – Essential parts of an FFT-based heterodyne receiver Figure 193 – Dynamic range for broadband emission as measured with the peak detector Figure 194 – Set-up of FFT-based system type 2 Figure 195 – FFT Software ("FFTemi") screen shot Figure 196 – Example of pulse generator measurement with antenna Figure 197 – Radiated emission measurement of a motor – peak detector Figure 198 – Angular characterization of a PC Figure 199 – Example FFT IF analysis display	21
Figure 187 – Real-time FFT-based measuring instrument Figure 188 – Digital down converter Figure 189 – Short time fast Fourier transform – An example of implementation Figure 190 – Floating-point analogue-to digital conversion Figure 191 – Example of a 120 kHz Gaussian filter Figure 192 – Essential parts of an FFT-based heterodyne receiver Figure 193 – Dynamic range for broadband emission as measured with the peak detector Figure 194 – Set-up of FFT-based system type 2 Figure 195 – FFT Software ("FFTemi") screen shot Figure 196 – Example of pulse generator measurement with antenna Figure 197 – Radiated emission measurement of a motor – peak detector Figure 198 – Angular characterization of a PC Figure 199 – Example FFT IF analysis display	21
Figure 188 – Digital down converter	21
Figure 189 – Short time fast Fourier transform – An example of implementation Figure 190 – Floating-point analogue-to-digital conversion Figure 191 – Example of a 120 kHz Gaussian filter Figure 192 – Essential parts of an FFT-based heterodyne receiver Figure 193 – Dynamic range for broadband emission as measured with the peak detector Figure 194 – Set-up of FFT-based system type 2 Figure 195 – FFT Software ("FFTemi") screen shot Figure 196 – Example of pulse generator measurement with antenna Figure 197 – Radiated emission measurement of a motor – peak detector Figure 198 – Angular characterization of a PC Figure 199 – Example FFT IF analysis display	21
Figure 190 – Floating-point analogue-to-digital conversion Figure 191 – Example of a 120 kHz Gaussian filter Figure 192 – Essential parts of an FFT-based heterodyne receiver Figure 193 – Dynamic range for broadband emission as measured with the peak detector Figure 194 – Set-up of FFT-based system type 2 Figure 195 – FFT Software ("FFTemi") screen shot Figure 196 – Example of pulse generator measurement with antenna Figure 197 – Radiated emission measurement of a motor – peak detector Figure 198 – Angular characterization of a PC Figure 199 – Example FFT IF analysis display	21
Figure 191 – Example of a 120 kHz Gaussian filter Figure 192 – Essential parts of an FFT-based heterodyne receiver Figure 193 – Dynamic range for broadband emission as measured with the peak detector Figure 194 – Set-up of FFT-based system type 2 Figure 195 – FFT Software ("FFTemi") screen shot Figure 196 – Example of pulse generator measurement with antenna Figure 197 – Radiated emission measurement of a motor – peak detector Figure 198 – Angular characterization of a PC Figure 199 – Example FFT IF analysis display	21
Figure 192 – Essential parts of an FFT-based heterodyne receiver Figure 193 – Dynamic range for broadband emission as measured with the peak detector Figure 194 – Set-up of FFT-based system type 2 Figure 195 – FFT Software ("FFTemi") screen shot Figure 196 – Example of pulse generator measurement with antenna Figure 197 – Radiated emission measurement of a motor – peak detector Figure 198 – Angular characterization of a PC Figure 199 – Example FFT IF analysis display	21
Figure 192 – Essential parts of an FFT-based heterodyne receiver Figure 193 – Dynamic range for broadband emission as measured with the peak detector Figure 194 – Set-up of FFT-based system type 2 Figure 195 – FFT Software ("FFTemi") screen shot Figure 196 – Example of pulse generator measurement with antenna Figure 197 – Radiated emission measurement of a motor – peak detector Figure 198 – Angular characterization of a PC Figure 199 – Example FFT IF analysis display	21
Figure 194 – Set-up of FFT-based system type 2	22
Figure 195 – FFT Software ("FFTemi") screen shot	22
Figure 195 – FFT Software ("FFTemi") screen shot	22
Figure 197 – Radiated emission measurement of a motor – peak detector Figure 198 – Angular characterization of a PC	
Figure 198 – Angular characterization of a PC Figure 199 – Example FFT IF analysis display	22
Figure 199 – Example FFT IF analysis display	22
	22
	22
Figure A.1 – Example plot using the expression $P_{t} + G = P_{q} + 2$	23
Figure A.2 – Examples of a number of microwaves measured for P_{q} and P_{t}	
Figure B.1 – Definition of the ring-shaped area round the transmitter T	24
Figure C.1 – The permissible ranges of U_{h} and G are within the polygon $\{G_{L}, U_{a}\}$, $\{G_{L}, U_{d}\}$, $\{G_{U}, U_{d}\}$, $\{G_{I}, U_{C}\}$ and $\{G_{L}, U_{a}\}$. For the given value U_{L} the double-shaded area represents $pr\{U_{h} \geq U_{L}\}$	
Figure F.1 – Vertical radiation patterns of horizontally polarized fields, 109 MHz, 300 m scan radius (adapted from [34])	24

Figure F.3 – Vertical radiation patterns of horizontally polarized fields, 109 MHz, 300 m scan radius (adapted from [34])	256
Figure F.4 – Vertical radiation patterns of horizontally polarized fields, 109 MHz, 300 m scan radius (adapted from [34])	
((
Table 1 – Comparative response of slideback peak, quasi-peak and average detectors to sine wave, periodic pulse and Gaussian waveform	22
Table 2 – Characteristics of gate generator and modulator to simulate various types of broadband interference	28
Table 3 – Summary results of building-effect, A _b , analysis	38
Table 4 – Summary of results of <i>G</i> -factor analysis	41
Table 5 – Summary of Lo factors (far-field)	41
Table 6 – Summary of truncation parameters of $f(G)$	
Table 7 – Summary results of equivalent-resistance analysis	43
Table 8 – Example of field-strength classification	
Table 9 – Example of voltage classification assuming for the outdoor field strength: $E_{\rm max}$ = 60 V/m and $E_{\rm min}$ = 0,01 V/m	47
Table 10 – Summary of the parameters used in the numerical examples presented in Figures 16 and 17	51
Table 11 – Frequencies of interest in ITU designated bands from Table 9 of CISPR 11:2009	58
Table 12 – Electrical constants for "medium dry ground" [31] (CCIR: medium dry ground; rocks; sand; medium sized towns[32])	59
Table 13 – Electrical constants for "wet ground" [31] (CCIR: marshes (fresh water); cultivated land [24]) and "very dry ground" [31] (CCIR: very dry ground; granite mountains in cold regions; industrial areas [32]).	59
Table 14 – Estimates of the errors in prediction of radiation in vertical directions based on a measurement height scan from 1 m to 4 m at known distances, d; frequency = 75 MHz (adapted from [39])	-16-3-201 67
Table 15 – Estimates of the errors in prediction of radiation in vertical directions based on a measurement height scan from 1 m to 4 m at known distances, d; frequency = 110 MHz (adapted from [39])	71
Table 16 – Estimates of the errors in prediction of radiation in vertical directions based on a measurement height scan from 1 m to 4 m at known distances, d; frequency = 243 MHz (adapted from [39])	
Table 17 – Estimates of the errors in prediction of radiation in vertical directions based on a measurement height scan from 1 m to 4 m at known distances, d; frequency = 330 MHz (adapted from [39])	
Table 18 – Estimates of the errors in prediction of radiation in vertical directions based on a measurement height scan from 1 m to 4 m at known distances, <i>d</i> ; frequency = 1 000 MHz (adapted from [39])	
Table 19 – Predictability of radiation in vertical directions at 100 kHz, using ground-based measurements of horizontally oriented <i>H</i> -field at distances up to 3 km from the source (figures are located in 4.6.8)	101
Table 20 – Predictability of radiation in vertical directions at 1 MHz, using ground-based measurements of horizontally oriented <i>H</i> -field at distances up to 300 m from the source (figures are located in 4.6.8)	103
Table 21 – Predictability of radiation in vertical directions at 10 MHz, using ground-based measurements of horizontally oriented <i>H</i> -field at distances up to 300 m from the source (figures are located in 4.6.8)	104